Experimental and numerical analysis of jet penetration and gas evolution in a single-nozzle distributor fluidised bed

Luca Panariello[a], Domenico Macrí[a], Valerio Zito[a,b], Roberto Solimene[b], Piero Salatino[b], Paola Lettieri[a], Massimiliano Materazzi[a]

[a] *Department of Chemical Engineering, University College London, Torrington Place, London WC1E 7JE, UK*
[b] *Dipartimento di Ingegneria Chimica, dei Materiali e della Produzione Industriale, Universita' degli Studi di Napoli Federico II, P.le Tecchio, 80-80125 Napoli, Italy*

ABSTRACT

This paper studies from experimental and theoretical perspectives the injection of gas in a stagnant solid bed via horizontal nozzles to analyse the formation of permanent jet plumes and subsequent bubbles detachment. Advanced 3D X-Ray imaging techniques have been developed and used to observe the phenomenon, as well as to quantify important process parameters (gas distribution, jet length, bubble size, etc.). The experimental results are compared with those obtained from three-dimensional computational fluid dynamics (CFD) simulations of a gas-solid fluidized bed with primary air injection performed through a two-orifice horizontal nozzle. The proposed model correctly predicts the jet penetration at all the jet velocities tested. Uneven distribution of air through the cross-section of the bed is also observed, with the presence of the same two distinct regions experimentally observed, namely a fluidized core region and a compacted peripheral region. However, the model fails in predicting jet interaction and curvature due to asynchronous bubbles detachment from the jets. This study demonstrates the usefulness of X-ray radiography in noninvasively visualizing detailed internal features of industrial fluidized

beds. These results will be used in future studies to refine CFD simulations for 3D fluidised bed systems.

Keywords:

X-ray imaging; Fluidised beds; Gas nozzles; Gas Jets

1. INTRODUCTION

Fluidised beds are among the most popular reactor designs for use in energy and chemical processing industries. The biggest advantage they provide relates to the high heat-transfer rates and good phase-mixing which, notably, give them uniform bed temperatures across the reactor. This feature makes them particularly suitable for high-temperature processes, especially those associated to the recent advances of low-carbon technologies, such as gasification of biomass and regeneration of nuclear waste [1,2]. The common assumption in these industrial cases is that no hot spot establishes in the reactor, as strong back mixing leads to uniform distribution of temperature. However, when faced with a highly exothermic reaction, significant temperature gradients may occur, especially for those confined regions where particle motion and gas distribution are poor and, consequently, hot spots could develop. The lack of vigorous motion in these areas allows time for permanent bonds between the particles to form through sintering, which in most cases lead rapidly to the defluidization of the system [3,4]. The gas distributor in these reactors is understandably one of the key elements to control so as to warrant uniform and stable fluidization across the entire bed, and therefore minimise the risk of hot spots. Various gas distributors are employed industrially, depending on the characteristics and the necessities of

the process [5]. The most common type of distributor in small scale reactors is the distributor plate due to its simplicity and ease of fitting between flanges. This, however, suffers from different drawbacks, in particular, the requirement of a high pressure underneath to minimize solid weepage to the plenum and thermal distortion at high temperatures [5,6]. Consequently, in many industrial applications, other options are adopted. Among these, the 'nozzle standpipe' is of high relevance. In this distributor, gas (in most cases hot air or steam) is introduced into the bed as vertical or horizontal jets at certain heights above the base of the reactor creating a high turbulent region with enhanced mixing of gas and solids. If the nozzles are correctly spaced and the holes adequately sized, this type of distributor gives excellent fluidization and allows long term operation, even at high temperatures [5,6]. The design of the nozzle standpipe distributor is rather complex, mostly due to the lack of empirical relations which take into account different scales of application [7]. The injection of gas in a stagnant solid bed via horizontal nozzles results in the formation of a permanent jet plume from which bubbles detach and rise in the bed. Chen and Weinstein [8] measured the penetration and shape formed by a horizontal jet in a rectangular fluidized bed, showing that horizontal jets form three regions: the jetting region, the bubble region and a surrounding compaction zone. Several correlations for predicting the penetration lengths of horizontal gas jets in fluidised beds have been developed [9–15]. Most of these studies are based on direct visual observation of jets using photographic or high-speed cine-film analysis, showing that the jet penetration length increases with increasing velocity of gas injection in gas-solid fluidized beds. However, due to the limitations of the experimental techniques, these studies had to be conducted on very thin reactors, implying significant walls interactions and, in turn, poor extrapolation of results to real systems [16,17]. The Authors have

overcome this problem by applying X-ray imaging for the analysis of jet penetration in large scale 3-D beds [18]. Based on the experimental data obtained, a new and improved empirical correlation to predict the jet penetration has been proposed, whose validity has been checked with a variety of gas velocities, particle densities and sizes.

The gas injected through the nozzle with an appropriate velocity detaches from the jet and determines the fluidization of the bed. Mapping the distribution of the gas injected from a nozzle in a stagnant bed is not trivial, as poorly fluidized regions reasonably coexist with well-fluidized parts; Chen and Weinstein [8] investigated the behaviour of a lateral injection of gas in a bi-dimensional fluidized bed, where a distributor plate fed the primary gas source. The results emphasized the changes in the voidage of the region surrounding the gas injection, highlighting the presence of a compacted region where the voidage is smaller than that establishing before gas injection. This mechanism, which takes place when the nozzle represents the primary source of gas in the bed, would result in the presence of poorly fluidized regions in the bed: consequently, it is common practice to employ a relatively large number of nozzles to fluidize a single bed. However, optimizing the number of nozzles is a rather challenging operation, in particular, due to limits related to different scales of applications between the lab and the final reactors. This eventually results in an overestimation of the number of nozzles required as distributors, leading to a cost increase of the reactor.

In this work, we analyse the gas distribution in the bed generated by primary injections via nozzle-type distributors, using non-invasive X-ray imaging technique. We also investigate the possibility offered by typical CFD models in simulating this kind of systems, as numerical modelling could represent a useful aid for the design and optimization of nozzles-type gas distributors in industrial

reactors. To date, CFD simulations have been mainly performed to describe systems where the primary gas injection is established through a perforated plate. In most cases, gas jets have been simulated when used for secondary gas injections [19,20] or in the case of spouted beds [21–24]. For example, Hong *et al.* [11] performed two-dimensional simulations to study the inclined jet penetration of secondary gas injections into a fluidized bed. However, the two-dimensional approximation of the domain is not justifiable due to the inherent three-dimensional features of the simulated system [19]. In literature, only a few three-dimensional CFD simulations of fluidized beds are available [19,25–28], mostly due to their high computational cost. Nonetheless, their results show better agreement with experimental data, hence they are becoming increasingly popular for industrial applications.

This study aims at investigating the gas distribution generated by a two-orifice nozzle in a 3-D fluidized bed reactor through X-ray imaging, with emphasis on the coexistence of non-fluidized regions despite operating the bed at gas superficial velocities above incipient fluidization. The non-intrusive nature of the technique employed gives confidence that the observed gas distribution and jet penetration lengths are accurate and not affected by measurement artefacts that may jeopardize alternative methods. Finally, we compare the experimental results with those obtained from a 3-D CFD simulation of the bed, highlighting the degree to which the proposed model is able to reproduce the phenomenology of gas injection and distribution.

2. MATERIALS AND METHODS

2.1 Experimental

A 150 mm ID Perspex square reactor has been employed as a fluidization column. Technical air at 5 bars is injected in the bed using a two-orifice industrial-scale nozzle, located along the axis of the column, at the height of 25 cm from the bottom. The nozzle is realized in Acrylonitrile-Butadiene-Styrene with a 3D printer and is characterized by an orifice diameter d_0 = 4.1 mm. A schematic representation of the fluidized bed and the main features of the nozzle are outlined in Figure 1.

A high-power pulsed X-ray system [18,29] has been employed to record the images in the jetting area. The X-Ray system is a non-intrusive analysis tool that can provide a detailed insight of multiphase systems that would be otherwise inaccessible. The X-Ray pulses pass through the vessel, or the reactor of interest, while an image-detecting device (Image intensifier + Camera) captures the pulses at a certain frequency. When the X-Rays pass through a material they get attenuated through scattering, absorption and reflection processes depending on the material interposed on its path: a grayscale image will be generated where black represents a full absorbing material on the path of the X-Ray and white is almost complete void. Given that different materials result in different absorption, the multiphase distribution in the vessel or the reactor can be deducted.

The image-capturing device is a standard 30 cm Industrial X-Ray Image Intensifier, and it is composed of a scintillator input window, a photocathode, electron optics, a luminescent screen and an output window. The image intensifier can detect and amplify the radioactive beam

emerging from the vessel, which is then converted into a grayscale image and recorded by a 1024 x 1024 pixel high-speed charge-coupled device (CDD) camera at 72 frames-per-second. The configuration of the X-ray system and the rig used in this study are outlined in Figure 1.

The material tested was sand, with particle density $\rho_p = 2500\ \mathrm{kg/m^3}$ and particle size $d_p = 200\ \mu\mathrm{m}$. This powder belongs to the Group B of Geldart classification of powders [30], hence the minimum fluidization velocity u_{mf} and the minimum bubbling velocity u_{mb} are approximately equal. The incipient fluidization velocity has been computed according to Wen and Yu [31], and is equal to u_{mf} = 4.6 cm/s.

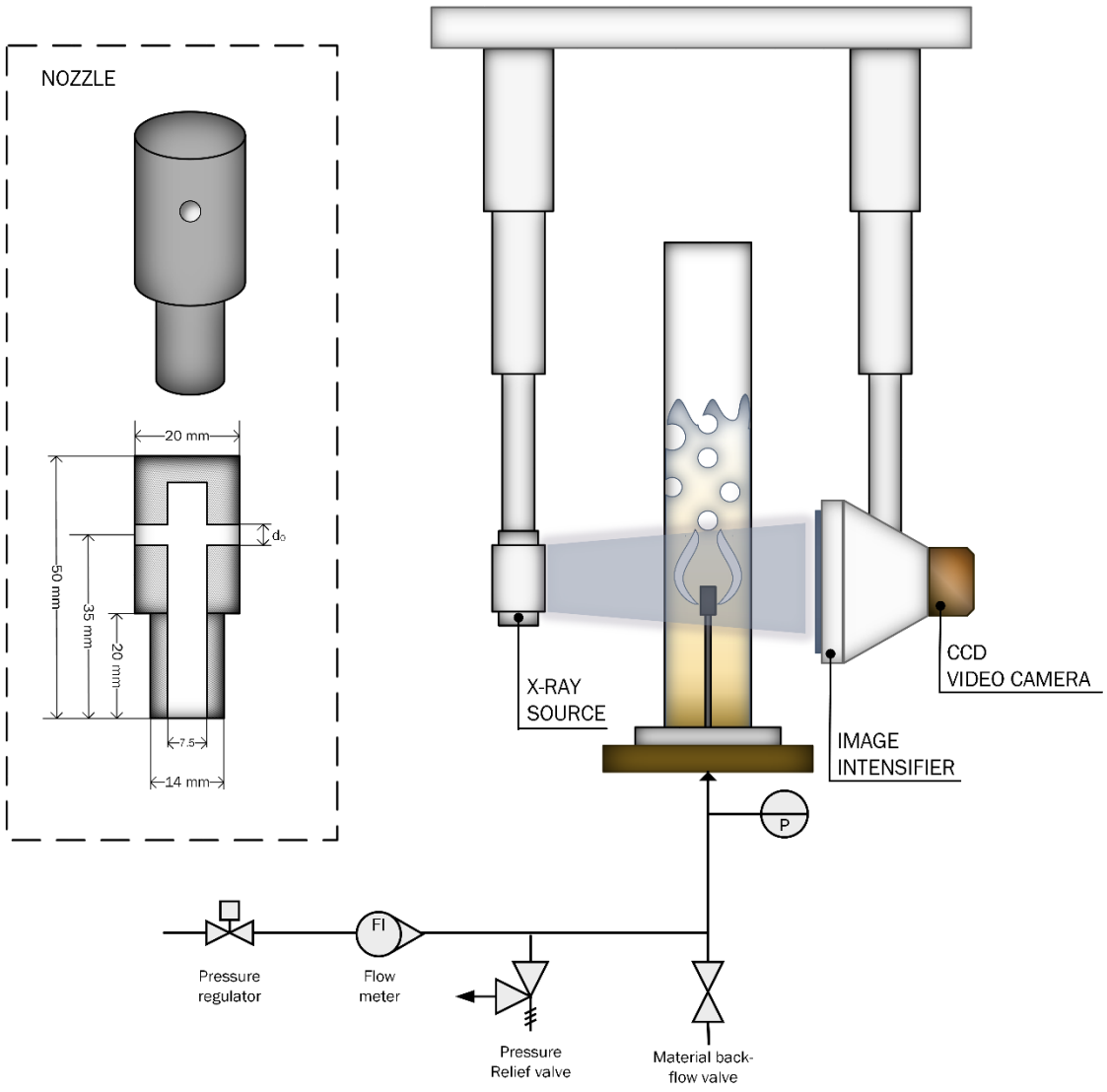

Figure 1 – Schematic of the nozzle (left side), the experimental rig and the X-ray configuration (right side)

The static height of the bed was $H_0 = 65$ cm from the bottom of the bed, which corresponds to a bed of 40 cm above the nozzle level. Images were recorded at different flow rates, which correspond to different jet velocities $v_j = Q/(\pi\, d_o^2/4\, n)$, where Q is the flow rate, d_o is the orifice diameter and n is the number of orifices. Values of flow rates in the range between 20 L/min and

80 L/min have been tested. The flow rate was set to the maximum value (80 L/min) and then decreased by 5 L/min in each experiment, down to the minimum value tested (20 L/min).

The resolution of the images obtained with the X-ray system allowed visualising and measuring the horizontal jet penetration (L_j) frame by frame. Jet penetration has been measured for both left and right jet at different jet velocities.

Specific scripts for the quantitative analysis of the bed height, the average fluid-bed voidage and the voidage distribution have been developed by using different built-in MATLAB functions. With particular regard to the bed voidage evaluation, the procedure extendedly reported by Yates and co-workers [32] that is based on the Beer-Lambert relationship between the attenuation of the X-ray beam and the resulting image intensity, was used

$$I = I_0 \exp\left(-\mu_m \rho_b l\right) \quad (1)$$

where I is the X-ray energy recorded by a detector, μ_m is the mass absorption coefficient for the material, ρ_b is the material density, and l is the X-ray path length through the medium. Typical medical-type X-Ray systems produce 2D images that are 2D "shadow" images of a 3D object. Since most of industrial nozzle applications involve multiple jets that evolve in space and time, a 3D representation could help revealing important details on the interphase between gas and emulsion phases. A stereographic method has been employed in this work to reconstruct the 3D shapes of the jets and bubbles for direct comparison with 3D CFD models. In this work, the reactor was rotated in front of the X-Ray imaging system, while recording the internal flow pattern from multiple angles. Each point of view was recorded for 10 seconds at a rate of 36

frames per second (fps), then an average image representative of the 360 total ones for each angle of view was generated through a specially designed code. The various time-averaged images are then used to reconstruct the 3D model and the tomographies of the object of interest. The main objective of this methodology was to produce a model of a specific system from a finite number of its projections, in order to ease comparison with 3D images from CFD simulations.

2.2 The model

The proposed model is based on a Euler-Euler two-phase scheme where the two phases are treated as interpenetrating continua identified by their phase fraction. This model is commonly employed to simulate fluidized bed reactors. However, this model has not been successfully used yet in the description of the gas-fluidized bed where the primary gas injection is achieved with a standpipe nozzle. Model equations are listed in Tables 1.

A three-dimensional domain representative of the vessel was simulated (Figure 2), reproducing the same geometrical and operating conditions of the experimental phase described in Section 2.1. The vessel height was 1 m and its diameter 15 cm. Air was injected through a nozzle with a 2 cm diameter and two orifices of 4 mm diameter, whose centres are located at a height of 24 cm from the bottom of the bed. The static height of the bed was 65 cm. Since the geometry and flow conditions appeared to be symmetric with the plane going through the axes of the vessel and the nozzle, the symmetry condition [20] has been employed on the right vertical surface of the domain, representing this plane. This allowed simulating only half of the vessel, hence significantly decreasing the computational effort. A no-slip condition [33] was applied to the other vertical surfaces and the bottom surface. Mass fluxes through these surfaces were set to

zero. Air was injected through the nozzle orifice at three different velocities, respectively 30 m/s, 35 m/s and 40 m/s. To avoid numerical instabilities, the air injection velocity has been ramped up linearly in a two-second time.

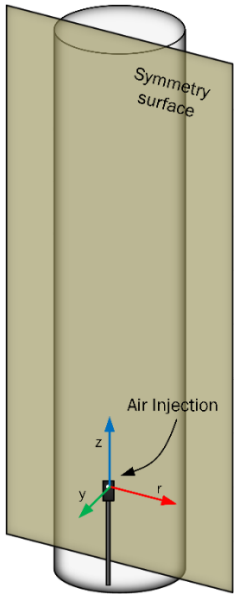

Figure 2 – Calculation domain and relevant boundary conditions

The commercial software Ansys Fluent 16 was used to integrate the model numerically. This code employs the finite volume method to convert the differential equations into a set of algebraic equations. Pressure and velocity were coupled with the Simultaneous Solution of Non-linearly Coupled Equation (SIMPLE) algorithm [34]. The time step was fixed at 0.0005 s [33,35]. A uniform grid with a grid size of 5 mm has been employed in the simulations. In literature, it has been reported that the grid size of 5 mm is sufficiently small for obtaining a grid-independent numerical solution for bubbling fluidized beds for both 2D and 3D simulations [25,33,36].

Table 1 - Model equations for CFD simulation

Continuity Equation	$\frac{\partial}{\partial t}(\alpha_i\rho_i) + \nabla\cdot(\alpha_i\rho_i\boldsymbol{v_i}) = 0$	
Momentum balance equation	$\frac{\partial}{\partial t}(\alpha_i\rho_i\boldsymbol{v_i}) + \nabla\cdot(\alpha_i\rho_i\boldsymbol{v_i}\boldsymbol{v_i}) = -\alpha_i\nabla \mathrm{p} + \nabla\cdot\boldsymbol{\tau_i} + \alpha_i\rho_i\boldsymbol{g} + \sum_{j=1}^{n} K_{drag}(\boldsymbol{v_j} - \boldsymbol{v_i})$	
Gas phase stress tensor	$\boldsymbol{\tau_g} = -\frac{2}{3}\mu_g tr(\boldsymbol{D_g})\boldsymbol{I} + 2\mu_g\boldsymbol{D_g}$	[37]
Fluid-solid drag coefficient	$K_{drag} = \frac{3}{4}\frac{\alpha_s\alpha_g\rho_g}{4\, v_{t,s}^2 d_p} C_D\left(\frac{Re_s}{v_{t,\,s}}\right)$	[38]
Terminal velocity for the solid phase	$v_{t,\,s} = 0.5(A - 0.06Re_s + \sqrt{(0.06Re_s)^2 + 0.12Re_s(2B - A) + A^2}$ $A = \alpha_g^{4.14}$ $B = \begin{cases} 0.8\alpha_g^{1.28}, & \alpha_g \le 0.85 \\ \alpha_g^{2.65}, & \alpha_g > 0.85 \end{cases}$	[39]
Drag function	$C_D = \left(0.63 + \frac{4.8}{\sqrt{Re_s/v_{t,s}}}\right)^2$	[40]
Solid phase stress tensor	$\boldsymbol{\tau_s} = -\left[p_s - \left(\lambda_s - \frac{2}{3}\mu_s\right)tr(\boldsymbol{D_s})\right]\boldsymbol{I} + 2\mu_s\boldsymbol{D_s}$	[41]
Granular temperature	$\frac{3}{2}\left[\frac{\partial}{\partial t}(\alpha_s\rho_s\Theta) + \nabla\cdot(\alpha_s\rho_s\boldsymbol{v_s}\Theta)\right] = \boldsymbol{\tau_s}:\nabla\boldsymbol{v_s} + \nabla\cdot(k_\Theta\nabla\Theta) - \gamma + \phi$ $\phi = -3K_{drag}\Theta$ $\gamma = \frac{12(1-e^2)g_0}{d_p\sqrt{\pi}}\rho_s{\alpha_s}^2\Theta^{\frac{3}{2}}$	[41]
Solid pressure	$p_s = 2\rho_s(1+e)\alpha_s^2 g_0\Theta$	[38]
Solid shear viscosity	$\mu_s = \frac{4}{5}\alpha_s\rho_s d_p g_0(1+e)\left(\frac{\Theta}{\pi}\right)^{1/2}\alpha_s + \frac{\alpha_s\rho_s d_p\sqrt{\Theta\pi}}{6(3-e)}\left[1 + \frac{2}{5(1+e)(3e-1)\alpha_s g_0}\right]$	[38]
Solid bulk viscosity	$\lambda_s = \frac{4}{3}\alpha_s^2\rho_s d_p g_0(1+e)\left(\frac{\Theta}{\pi}\right)^{1/2}$	[42]
Frictional stress	$\tau_s = \begin{cases} \tau_{s,k} & \alpha_s \le \alpha_f \\ \tau_{s,f} & \alpha_s > \alpha_f \end{cases}$	[38]
Frictional pressure	$p_{s,f} = \begin{cases} 0 & \alpha_s \le \alpha_f \\ 10^{25}\alpha_s(\alpha_s - \alpha_f) & \alpha_s > \alpha_f \end{cases}$	[38]
Frictional viscosity	$\mu_{s,f} = \frac{p_{s,f}\sqrt{2}\sin\varphi}{2\sqrt{\boldsymbol{D_s}:\boldsymbol{D_s}}}$	[43]

3. RESULTS AND DISCUSSION

3.1 Jets behaviour

The X-ray imaging technique allowed the direct observation of the hydrodynamics in the jetting area (**Error! Reference source not found.**). The images in Figure 3 show two distinct fluidizing jets. The two jets interact with each other by converging toward the axes of the reactor, forming a triangular structure above which bubbles break off. Subsequently, bubbles tend to rise along the reactor axis forming a bubble train. The two jets appeared stable in time, without any fluctuation in the penetration lengths. Surprisingly, bubbles started forming at a velocity well below the theoretical minimum fluidization condition, suggesting an uneven air distribution across the section of the reactor. The same hydrodynamic structure appeared at all the flow rates tested above minimum fluidization.

Figure 3 - Hydrodynamics evolution in the jetting region within 1.4 s, $v_j = 35\ m/s$

Voidage was measured from the recorded X-ray data by applying equation (1) to 720 images (corresponding to approximately 10 seconds recording), then converting the as obtained time-dependent voidage distribution into a single image, representative of the time-averaged voidage distribution (**Error! Reference source not found.**4). The experimental time-averaged voidage maps obtained do not allow a rigorous quantitative validation of the model since the values in the map are not representative of the pointwise alue of the voidage. In fact, by applying the Lambert-Beer model to the X-ray images, we only obtain values averaged across the chords corresponding to the depth of the bed. However, they enable a very accurate assessment of the hydrodynamic structures in the jetting area, which are identifiable in the experimental maps. The maps can also be easily compared with CFD results for a semi-quantitative validation.

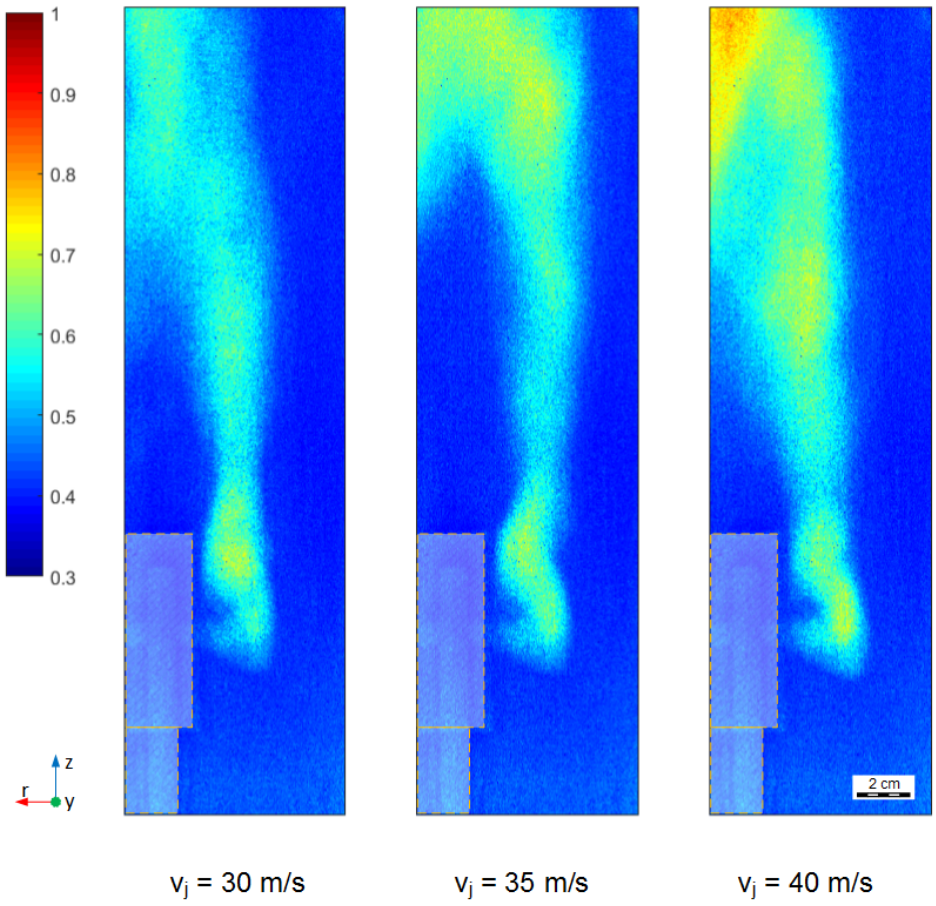

Figure 4 – Time-averaged voidage map experimentally determined.

Error! Reference source not found.(a) shows the time-averaged voidage contour at $v_j = 35\ m/s$ obtained from the simulation, for the right-side jet. A clear hydrodynamic pattern can be identified: air penetrates in the bed as a horizontal jet at the level of the two opposite nozzle orifices; it bends upwards by approximately 90° and generates a vertical line of bubbles. A specular trend is reproduced for the left side of the reactor due to the symmetry condition imposed by the model. Similar patterns have been recognized at all jet velocities simulated.

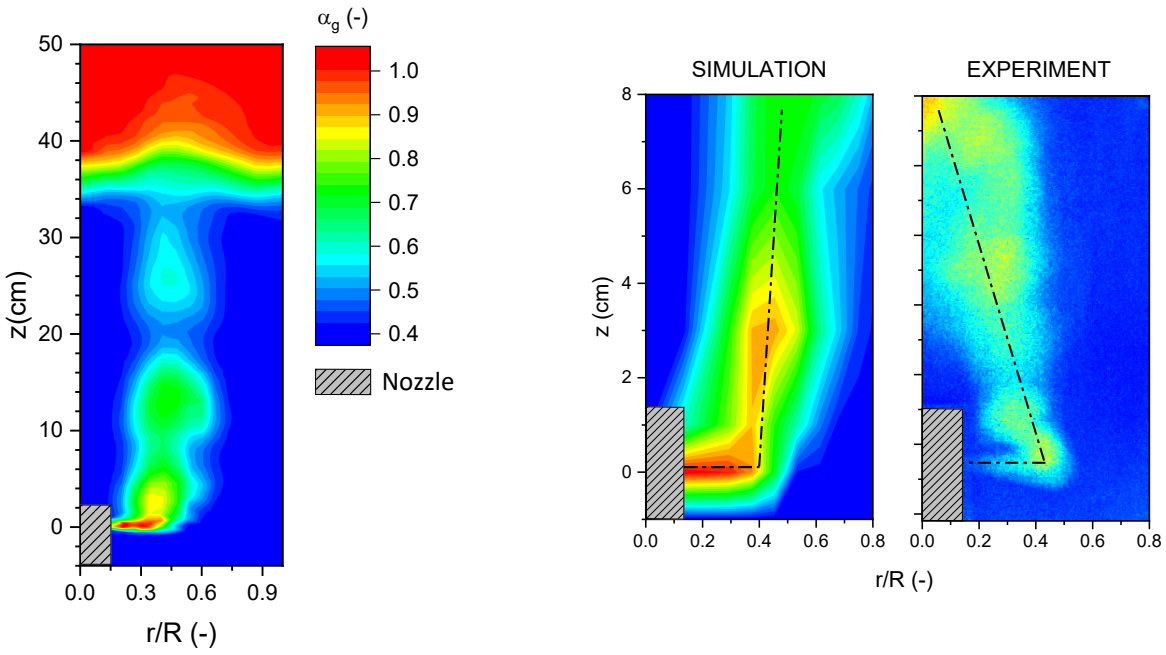

(a) (b)

Figure 5 – (a) Voidage contour from simulation in the x-z plane at $v_j = 35\ m/s$. (b) Hydrodynamics in the jetting region at $v_j = 35\ m/s$: computed voidage map compared with the experimental time-averaged voidage map, dashed lines show the curvatures of the

Error! Reference source not found.5(b) reports the direct comparison of the hydrodynamic structures in the jetting region comparing the computed voidage distribution with the experimental time-averaged voidage map. A sound reproduction of the jet is clearly obtained. However, the model seems to be failing in reproducing the curvature of the jets towards the central axis, as observed in the experiments.

This discrepancy might again be due to the use of the symmetry condition in the model, which separates the two jets and consider them completely independent from each other. Similar observations were made in other studies [44,45]. As a careful observation of the experimental

data suggests, bubbles detach in a non-synchronous manner from the jets plume, posing some doubts regarding the applicability of the symmetry condition (Video available in Supplementary Material). This asynchronous behaviour of the opposing jets leads to the migration of the bubbles towards the axis of the vessel, through a "leading-trailing" mechanism, where the pressure field determined by the first bubble allows the second bubble to follow the former, generating a single "train" of bubbles along the axis of the bed. Leading-trailing bubble mechanism is important in determining bubble size and flow pattern, and has previously been observed using other non-invasive techniques, such as MRI [46,47] and electrical capacitance tomography (ECT) [48]. However, this mechanism is ignored when a symmetry condition is applied, as observed in Figure 5, suggesting that a 3D simulation on the full domain would be more appropriate for an accurate reproduction of the hydrodynamics inside the bed. The modelling of multiple jets interaction and gas distribution in the spatial region above the nozzle will form part of a future, more detailed, X-Ray-CFD comparison study.

3.2 Jets penetration

To further support the last statement, we compared the experimental jet penetration with that obtained from the simulations. By defining the jet boundary at $\alpha_g = 0.8$ [11,49] jet penetration is measured frame by frame. The results of the simulations are then compared with the results and the proposed correlation reported in Panariello *et al.* [18]:

$$\frac{L_j}{d_o} = a\, Fr^b \frac{1}{\left(1 + \frac{d_p}{d_o}\right)^c} \left(\frac{\rho_0}{\rho_S}\right)^c \qquad (1)$$

Here L_j is the jet penetration, d_o is the nozzle diameter, Fr is the Froude number, d_p is the particle diameter, ρ_0 is the density of air, ρ_S is the particle density and a, b, c and d are fitting parameters, respectively equal to 61.2, 0.4, 5.6 and 0.4.

The correlation proposed in Panariello et al. was able to predict the jet penetration within 10% of the experimental value. As Figure 6 shows, simulations are in better agreement with the experimental results than the correlation. The latter was developed by correcting a pure hydrodynamic model (*i.e.* based solely on the Froude number) with the addition of "correcting factors" expressing the dependency of the jet penetration from particle density and size. A detailed mechanistic explanation of the inadequacy of the pure hydrodynamic model cannot be currently provided; however, the high value of c suggests that increasing d_p promotes gas leakage from the jet to the emulsion phase; modelling of gas leakage from bubbles shows that the fraction of gas escaping from the bubble depends not only on the particle size, but also on other parameters, as the gas flow rate and minimum fluidization velocity [50]. Interplay between the various parameters not accounted for in (1) could explain the improved accuracy obtained from the CFD simulations for the prediction of the jet penetration, also suggesting potential use of CFD modelling for the mechanistic study of jet penetration in stagnant beds.

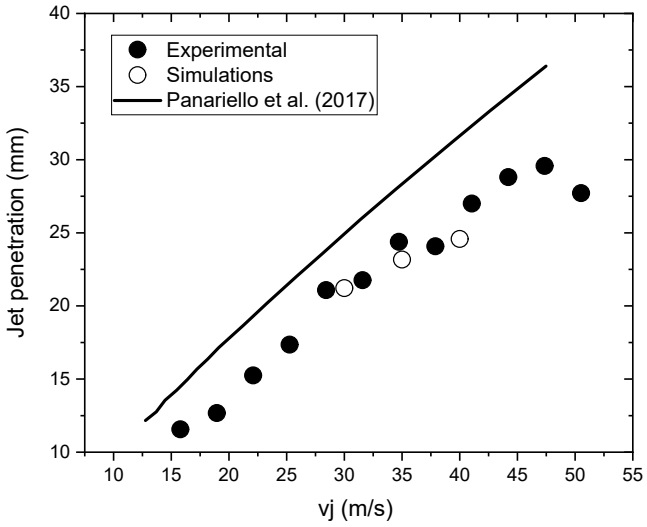

Figure 6 – Jet penetration at different jet velocities

3.2 Gas distribution

The voidage analysis from the X-ray images provides valuable insight into the quality of the gas distribution in the bed. By defining $\alpha_g = 0.43$ (i.e. the bed voidage at rest) as a threshold value between the fluidized and non-fluidized regions of the bed, it is possible to analyse how air distributes when jets are formed. Three different regions could be observed in the bed (Figure 5b), indicating that air distribution is not uniform across the bed. In particular, further to the jets area, we can observe an internal fluidised green region above the nozzle that contains the bubbles (r/R=0 - 0.4), and a peripheral, dark-blue region (r/R > 0.4) with values of solid fraction equal or even higher than that of the bed at rest, *i.e.* a compacted zone. This uneven gas distribution was expected and explains the observed discrepancy between the theoretical minimum fluidization flow rates, referred to the whole bed cross-section, and the experimentally

observed minimum fluidization condition. The presence of distinct regions in the bed is in agreement with other works [8]. This effect can be mitigated by increasing the number of jets maintaining the overall flowrate constant, as observed by [51].

CFD simulations do confirm the presence of a peripheral compacted region and a fluidised core region, with the boundary between the two located at approximately r/R = 0.2 - 0.6 (depending on the flow rate). A very good matching was observed for the region at nozzle level or immediately above (z=2 cm). This is even more evident when looking at different sections of the bed obtained from the stereography technique (Figure 7), and their comparison with CFD modelling results at the same conditions ($v_j = 35\ m/s$). Three-dimensional images are viewed using the methodology described inb Section 2.1. Additionally, the method can generate "slices" of the 3D image to produce 2D images of any section within the reactor. It could be observed that in the region immediately above the noozle (z=2cm), the bed behaves mostly as packed, with the exception of two distinct zones generated by continuous bubbling (local voidage comprised between 0.7 and 0.85). Local voidage values can be extracted from the qualitative voidage maps to produce quantitative graphs of the local time-averaged gas holdup along different heights through the reactor (Figure 8).

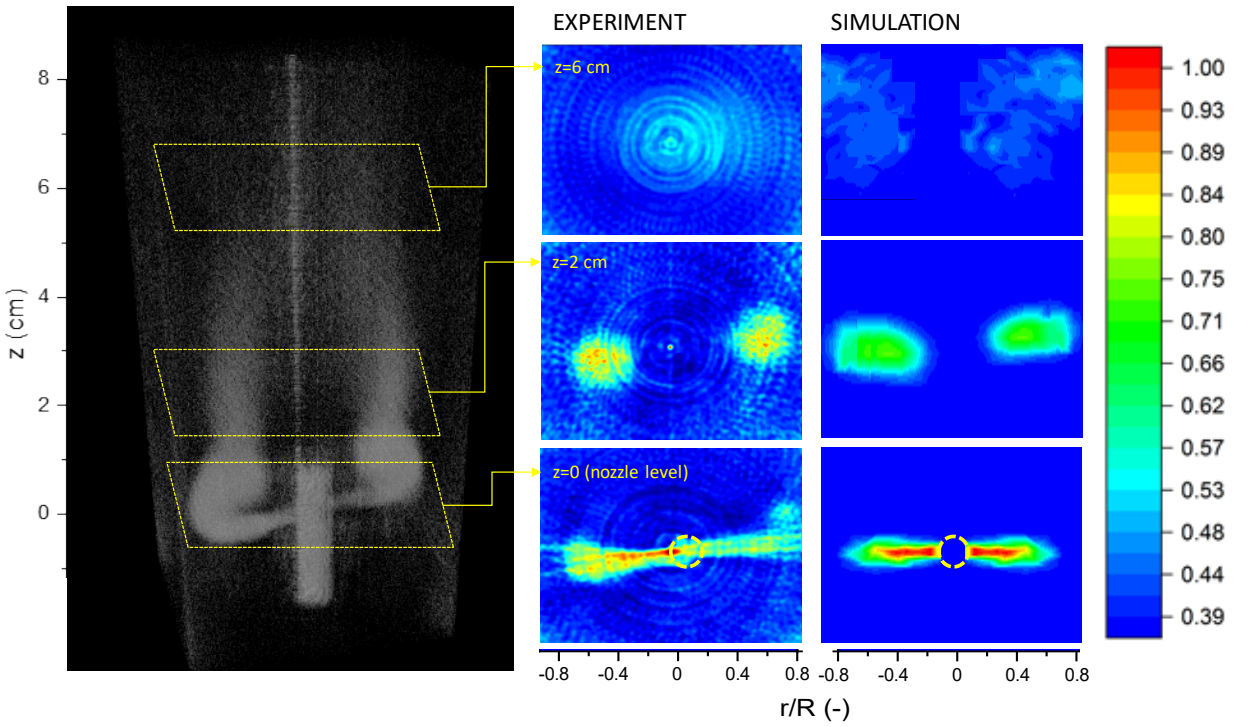

Figure 7 –3D reconstruction from X-ray images (time-averaged images at $v_j = 35\ m/s$), and comparison with CFD simulations at different heights (z = 0, 2, 6 cm) above the nozzle.

Good similarity can be observed between experimental and modelling results in the area close to the distributor (z=0-4 cm). Worse agreement is observed when looking at the gas distribution at higher heights of the bed (> 6 cm). This region appears with two distincts gas-rich zones on the sides of the square section generated by the CFD model, while centrally fluidized in the experiments. As previously stated, the numerical simulations seems to fail the prediction of the phenomenon of bubble migration towards the reactor axis, leading to poor predictability of the local gas distribution in this area. Nevertheless, average values across the entire section are very close, and in line with other studies [52]. The similarity in instantaneous gas-solid distributions

between the experiments and simulations in the area near the distributor provides confidence in the computational modelling, although a more refined version without symmetry condition is required for more accurate predictions at higher levels.

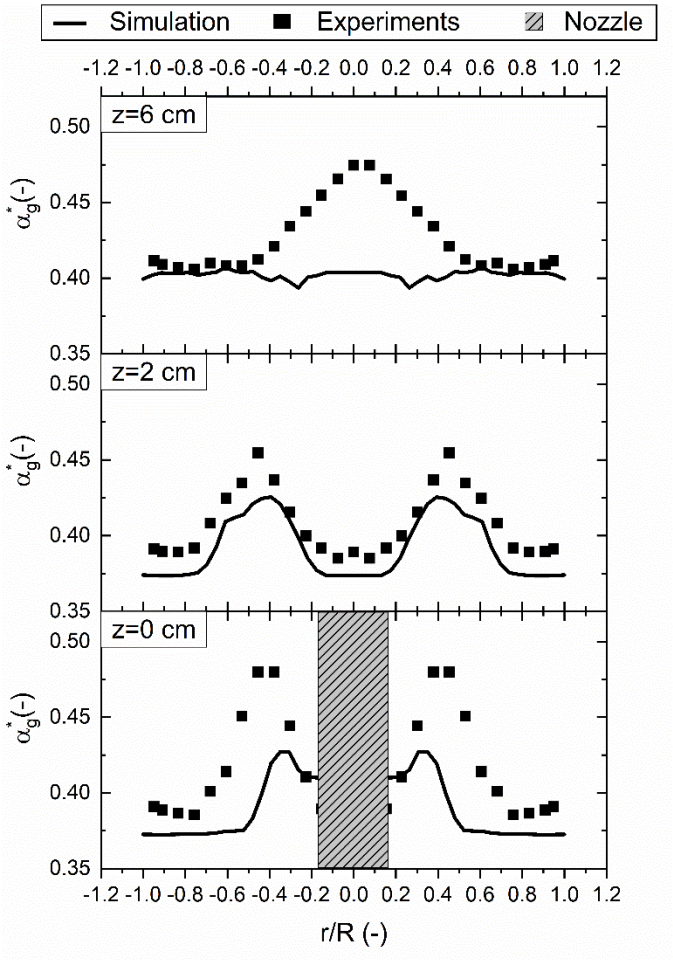

Figure 8 – Modelled and experimental time-averaged void fraction profiles (at $v_j = 35\ m/s$), at different heights (z = 0, 2, 6 cm) above the nozzle.

4. CONCLUSIONS

An analysis of the gas distribution in a 3-D fluidized bed was carried out with the use of an X-ray imaging system. Gas was introduced in the bed through a two-orifice nozzle-type distributor. The use of X-ray imaging allows the direct observation of the hydrodynamics of the bed, particularly important when studying the gas injection area to identify potential risk of localized solids stagnation and hot spots. This study highlighted the presence of a fluidized core consisting in a trail of rising bubbles, and an outer annular region where the powder is instead compacted. The experimental results are compared with those obtained from three-dimensional simulations of a gas-solid fluidized bed with primary air injection performed through a two-orifice horizontal nozzle. The proposed model correctly predicts the jet penetration at all the jet velocities tested. Uneven distribution of air through the cross-section of the bed is also observed, with the presence of the same two distinct regions that were experimentally observed, namely a fluidized core region and a compacted peripheral region. The model fails in predicting jet interaction and curvature. Further studies are intended to tackle this problem by removing the symmetry condition employed in this work, believed to be the main reason of discrepancy of the simulations from the experimental observations, due to the observed asynchrony of bubble detachment.

List of symbols:

Symbol	Description	Value	Ref.	Units
Alphabetic				
C_D	Drag coefficient			dimensionless
d_0	Nozzle diameter	$4 \cdot 10^{-3}$		m
d_p	Particle diameter	$2 \cdot 10^{-4}$		m
D	Vessel diameter	0.15		m
$\mathbf{D}$	Strain rate tensor			1/s
e	Coefficient of restitution	0.9	[53]	dimensionless
g	Gravitational acceleration	9.81		m/s^2
g_0	Radial distribution coefficient		[38]	dimensionless
H	Vessel height	1		m
H_s	Static bed height	0.65		m
k_Θ	Diffusion coefficient for granular energy		[38]	dimensionless
K_{drag}	Interphase exchange coefficient			dimensionless
P	Pressure			Pa
Re	Reynolds number			dimensionless
t	Time			s
Greek letters				
α	Volume fraction			dimensionless
α_0	Initial solid volume fraction	0.57		dimensionless
γ	Collision dissipation of energy			kg/s^3m
Θ	Granular temperature,			m^2/s^2
$\mathbf{I}$	Identity tensor			dimensionless
λ	Bulk viscosity			Pa s
μ	Shear viscosity			Pa s
ν	Velocity			m/s
ρ	Density			kg/m^3

ρ_s	Particle density	2500	kg/m^3
$\boldsymbol{\tau}$	Stress tensor		Pa
φ	Angle of internal friction		Deg
Φ	Transfer rate of kinetic energy		kg/s^{3}m
Subscripts			
f	Friction		dimensionless
g	Gas phase		dimensionless
i	Either fluid or solid phase		dimensionless
k	Kinetic		dimensionless
p	Particle		dimensionless
s	Solid phase		dimensionless

5. REFERENCES

[1] S. Iannello, S. Morrin, M. Materazzi, Fluidised Bed Reactors for the Thermochemical Conversion of Biomass and Waste, KONA Powder Part. J. (2020). https://doi.org/10.14356/kona.2020016.

[2] J.G. Yates, P. Lettieri, Fluidized-Bed Reactors: Processes and Operating Conditions, Springer International Publishing, Cham, 2016. https://doi.org/10.1007/978-3-319-39593-7.

[3] D. Macrì, S. Sutcliffe, P. Lettieri, Fluidized bed sintering in TiO2 and coke systems, Chem. Eng. J. (2020). https://doi.org/10.1016/j.cej.2019.122711.

[4] M. Materazzi, Gasification of Waste Derived Fuels in Fluidized Beds: Fundamental Aspects and Industrial Challenges, in: Clean Energy from Waste, Springer Theses, 2017: pp. 19–63.

[5] W.-C. Yang, Handbook of fluidization and fluid-particle systems, 2003.

[6] D. Kunii, O. Levenspiel, Fluidization Engineering, 1991.

[7] D. Newton, Revealing the secrets of fluidised beds Exploiting links between academia and industry, Ingenia. (2004) 47–52.

[8] L. Chen, H. Weinstein, Shape and Extent of the Void Formed by a Horizontal Jet in a Fluidized Bed, AIChE J. 39 (1993) 1901–1909.

[9] J. Benjelloun, F. V., Determination des longueurs de jets de gaz horizontaux dans des lits fluidises, in: 6emes Journees Eur. Sur La Fluid., 1991: pp. 108–115.

[10] C. Briens, F. Berruti, L. Feng, J. McMillan, The 13th International Conference on Fluidization - New Paradigm in Fluidization Engineering, Fluid. Nanopowders Exp. Model. Appl. (2010).

[11] R. Hong, H. Li, H. Li, Y. Wang, Studies on the inclined jet penetration length in a gas-solid fluidized bed, Powder Technol. 92 (1997) 205–212. https://doi.org/10.1016/S0032-5910(97)03238-5.

[12] L. Massimilla, GAS JETS IN FLUIDIZED BEDS., 1985.

[13] J.M.D. Merry, Penetration of vertical jets into fluidized beds, AIChE J. (1975). https://doi.org/10.1002/aic.690210312.

[14] N.A. Shakhova, Discharge of turbulent jets into a fluidized bed, J. Eng. Phys. (1968). https://doi.org/10.1007/BF00826970.

[15] K. Zhang, P. Pei, S. Brandani, H. Chen, Y. Yang, CFD simulation of flow pattern and jet penetration depth in gas-fluidized beds with single and double jets, Chem. Eng. Sci. (2012). https://doi.org/10.1016/j.ces.2011.09.018.

[16] M. Pore, G.H. Ong, C.M. Boyce, M. Materazzi, J. Gargiuli, T. Leadbeater, A.J. Sederman, J.S. Dennis, D.J. Holland, A. Ingram, P. Lettieri, D.J. Parker, A comparison of magnetic

resonance, X-ray and positron emission particle tracking measurements of a single jet of gas entering a bed of particles, Chem. Eng. Sci. 122 (2015) 210–218. https://doi.org/10.1016/j.ces.2014.09.029.

[17] J.G. Yates, S.S. Cobbinah, D.J. Cheesman, S.P. Jordan, Particle attrition in fluidized beds containing opposing jets, in: AIChE Symp. Ser., 1991.

[18] L. Panariello, M. Materazzi, R. Solimene, P. Salatino, P. Lettieri, X-ray imaging of horizontal jets in gas fluidised bed nozzles, Chem. Eng. Sci. 164 (2017) 53–62. https://doi.org/10.1016/j.ces.2017.01.055.

[19] T. Li, K. Pougatch, M. Salcudean, D. Grecov, Numerical simulation of single and multiple gas jets in bubbling fluidized beds, Chem. Eng. Sci. 64 (2009) 4884–4898. https://doi.org/10.1016/j.ces.2009.07.024.

[20] T. Li, K. Pougatch, M. Salcudean, D. Grecov, Numerical simulation of horizontal jet penetration in a three-dimensional fluidized bed, Powder Technol. 184 (2008) 89–99. https://doi.org/10.1016/j.powtec.2007.08.007.

[21] C.R. Müller, D.J. Holland, J.F. Davidson, J.S. Dennis, L.F. Gladden, A.N. Hayhurst, M.D. Mantle, A.J. Sederman, Geometrical and hydrodynamical study of gas jets in packed and fluidized beds using magnetic resonance, Can. J. Chem. Eng. 87 (2009) 517–525. https://doi.org/10.1002/cjce.20191.

[22] D.J. Patil, M. Van Sint Annaland, J.A.M. Kuipers, Critical comparison of hydrodynamic models for gas-solid fluidized beds - Part I : Bubbling gas-solid fluidized beds operated with a jet, Chem. Eng. Sci. 60 (2005) 57–72. https://doi.org/10.1016/j.ces.2004.07.059.

[23] A. Passalacqua, L. Marmo, A critical comparison of frictional stress models applied to the

simulation of bubbling fluidized beds, Chem. Eng. Sci. 64 (2009) 2795–2806. https://doi.org/10.1016/j.ces.2009.03.005.

[24] D. Gidaspow, B. Ettehadieh, Fluidization in Two-Dimensional Beds with a Jet. 2. Hydrodynamic Modeling, Ind. Eng. Chem. …. (1983) 193–201. https://doi.org/10.1021/i100010a008.

[25] L. Cammarata, P. Lettieri, G.D.M. Micale, D. Colman, 2D and 3D CFD Simulations of Bubbling Fluidized Beds Using Eulerian-Eulerian Models, Int. J. Chem. React. Eng. 1 (2003). https://doi.org/10.2202/1542-6580.1083.

[26] E. Esmaili, N. Mahinpey, Adjustment of drag coefficient correlations in three dimensional CFD simulation of gas-solid bubbling fluidized bed, Adv. Eng. Softw. 42 (2011) 375–386. https://doi.org/10.1016/j.advengsoft.2011.03.005.

[27] N. Xie, F. Battaglia, S. Pannala, Effects of using two- versus three-dimensional computational modeling of fluidized beds. Part I, hydrodynamics, Powder Technol. 182 (2008) 1–13. https://doi.org/10.1016/j.powtec.2007.07.005.

[28] N. Xie, F. Battaglia, S. Pannala, Effects of using two- versus three-dimensional computational modeling of fluidized beds: Part II, budget analysis, Powder Technol. 182 (2008) 14–24. https://doi.org/10.1016/j.powtec.2007.09.014.

[29] P. Lettieri, J.G. Yates, New Generation X-ray Imaging for multiphase systems, 14th Int. Conf. Fluid. – From Fundam. to Prod. (2013).

[30] D. Geldart, Types of gas fluidization, Powder Technol. 7 (1973) 285–292. https://doi.org/10.1016/0032-5910(73)80037-3.

[31] C.Y. Wen, Y.H. Yu, A generalized method for predicting the minimum fluidization velocity,

AIChE J. 12 (1966) 610–612.

[32] S. Tebianian, N. Ellis, P. Lettieri, J.R. Grace, X-ray imaging for flow characterization and investigation of invasive probe interference in travelling fluidized bed, Chem. Eng. Res. Des. 104 (2015) 191–202. https://doi.org/10.1016/j.cherd.2015.08.006.

[33] C. Tagliaferri, L. Mazzei, P. Lettieri, A. Marzocchella, G. Olivieri, P. Salatino, CFD simulation of bubbling fluidized bidisperse mixtures: Effect of integration methods and restitution coefficient, Chem. Eng. Sci. 102 (2013) 324–334. https://doi.org/10.1016/j.ces.2013.08.015.

[34] S. Patankar, Numerical heat transfer and fluid flow, 1980. https://doi.org/10.1016/j.watres.2009.11.010.

[35] L. Mazzei, A. Casillo, P. Lettieri, P. Salatino, CFD simulations of segregating fluidized bidisperse mixtures of particles differing in size, Chem. Eng. J. 156 (2010) 432–445. https://doi.org/10.1016/j.cej.2009.11.003.

[36] T. McKeen, T. Pugsley, Simulation and experimental validation of a freely bubbling bed of FCC catalyst, Powder Technol. 129 (2003) 139–152. https://doi.org/10.1016/S0032-5910(02)00294-2.

[37] R.B. Bird, W.E. Stewart, E.N. Lightfoot, Transport Phenomena, Appl. Mech. Rev. 55 (2002) R1. https://doi.org/10.1051/jp4:20020462.

[38] M. Syamlal, W. Rogers, T.J. O`Brien, MFIX documentation theory guide, Other Inf. PBD Dec 1993. 1004 (1993) Medium: ED; Size: 49 p. https://doi.org/METC-9411004, NTIS/DE9400087.

[39] J. Garside, M.R. Al-Dibouni, Velocity-Voidage relationships for Fluidization and

Sedimentation, I EC Process Des. Dev. 16 (1977) 206–214.

[40] J.M. Dalla Valle, Micromeritics, Pitman, London, 1948.

[41] D. Gidaspow, Multiphase flow and fluidization, Academic Press, 1994. https://doi.org/10.1016/0377-0257(94)80007-3.

[42] C.K.K. Lun, S.B. Savage, D.J. Jeffrey, N. Chepurniy, Kinetic theories for granular flow: inelastic particles in Couette flow and slightly inelastic particles in a general flowfield, J. Fluid Mech. 140 (1984) 223. https://doi.org/10.1017/S0022112084000586.

[43] D.G. Schaeffer, Instability in the Evolution Equations Describing Incompressible Granular Flow, J. Diff. Eq. 66 (1987).

[44] R. Krishna, J.M. van Baten, Scaling up Bubble Column Reactors with the Aid of CFD, Chem. Eng. Res. Des. 79 (2001) 283–309. https://doi.org/10.1205/026387601750281815.

[45] C.C. Pain, S. Mansoorzadeh, C.R.E. De Oliveira, Study of bubbling and slugging fluidized beds using the two-fluid granular temperature model, Int. J. Multiph. Flow. 27 (2001) 527–551. https://doi.org/10.1016/S0301-9322(00)00035-5.

[46] H.T. Fabich, A.J. Sederman, D.J. Holland, Study of bubble dynamics in gas-solid fluidized beds using ultrashort echo time (UTE) magnetic resonance imaging (MRI), Chem. Eng. Sci. (2017). https://doi.org/10.1016/j.ces.2017.07.003.

[47] C.R. Müller, J.F. Davidson, J.S. Dennis, P.S. Fennell, L.F. Gladden, A.N. Hayhurst, M.D. Mantle, A.C. Rees, A.J. Sederman, Rise velocities of bubbles and slugs in gas-fluidised beds: Ultra-fast magnetic resonance imaging, Chem. Eng. Sci. (2007). https://doi.org/10.1016/j.ces.2006.08.019.

[48] T.C. Chandrasekera, Y. Li, D. Moody, M.A. Schnellmann, J.S. Dennis, D.J. Holland,

Measurement of bubble sizes in fluidised beds using electrical capacitance tomography, Chem. Eng. Sci. (2015). https://doi.org/10.1016/j.ces.2015.01.011.

[49] S.J. Gelderbloom, D. Gidaspow, R.W. Lyczkowski, CFD Simulations of Bubbling / Collapsing Fluidized Beds for Three Geldart Groups, 49 (2003).

[50] H.S. Caram, K.-K. Hsu, Bubble formation and gas leakage in fluidized beds, Chem. Eng. Sci. 41 (1986) 1445–1453.

[51] M. Materazzi, P. Lettieri, J.M. Dodds, A. Milliken, X-ray imaging for design of gas nozzles in large scale fluidised bed reactors, Powder Technol. 316 (2017). https://doi.org/10.1016/j.powtec.2016.12.089.

[52] M. Deza, N.P. Franka, T.J. Heindel, F. Battaglia, CFD modeling and x-ray imaging of biomass in a fluidized bed, J. Fluids Eng. Trans. ASME. (2009). https://doi.org/10.1115/1.4000257.

[53] N. Reuge, L. Cadoret, C. Coufort-Saudejaud, S. Pannala, M. Syamlal, B. Caussat, Multifluid Eulerian modeling of dense gas-solids fluidized bed hydrodynamics: Influence of the dissipation parameters, Chem. Eng. Sci. 63 (2008) 5540–5551. https://doi.org/10.1016/j.ces.2008.07.028.